

# Competition of Core-Shell and Janus Morphology in Alloy Nanoparticles: Insights From a Phase-Field Model

P. Pankaj, Saswata Bhattacharya\* and Subhradeep Chatterjee†

*Department of Materials Science and Metallurgical Engineering,*

*Indian Institute of Technology, Hyderabad, 502285, India.*

*Emails: ms15resch11005@iith.ac.in, saswata@msme.iith.ac.in, subhradeep@msme.iith.ac.in*

May 21, 2021

## Abstract

Bimetallic nanoparticles (BNPs) exhibit diverse morphologies such as core-shell, Janus, onion-like, quasi-Janus, and homogeneous structures. Although extensive effort has been directed towards understanding the equilibrium configurations of BNPs, kinetic mechanisms involved in their development have not been explored systematically. Since these systems often contain a miscibility gap, experimental studies have alluded to spinodal decomposition (SD) as a likely mechanism for the formation of such structures. We present a novel phase-field model for confined (embedded) systems to study SD-induced morphological evolution within a BNP. It initiates with the formation of compositionally modulated rings as a result of surface directed SD, and eventually develops into core-shell or Janus structures due to coarsening/breakdown of the rings. The final configuration depends crucially on contact angle and particle size - Janus is favored at smaller sizes and higher contact angles. Our simulations also illustrate the formation of metastable, kinetically trapped structures as a result of competition between capillarity and diffusion.

## 1 Introduction

Bimetallic nanoparticles (BNPs) are an important class of materials that exhibit novel chemical, optical, electrical, electronic, magnetic phenomena. A general overview of their methods of synthesis, structure and its underlying theoretical aspects, properties, and potential applications can be found, for example, in Ferrando et al.<sup>1</sup> and Gilroy et al.<sup>2</sup>, while more specific reviews concerning properties targeted to their catalytic<sup>3</sup>, plasmonic<sup>4</sup>, or magnetic<sup>5</sup> applications are also

---

\*Corresponding author.

†Corresponding author.

available. These properties in turn depend on the internal configuration of the nanoparticles (NPs), with core-shell (CS), onion-like rings and Janus (side-segregated/dumbbell-like) being the most frequently observed morphologies. BNPs have been synthesized in a wide range of systems such as Ag-Cu<sup>6-9</sup>, Ag-Ni<sup>10</sup>, Au-Co<sup>11,12</sup>, Au-Ni<sup>11,13</sup>, Au-Pd<sup>14</sup>, Co-Cu<sup>15</sup>, Co-Pt<sup>16</sup>, Cu-Mo<sup>17</sup> and Ni-Pt<sup>18</sup>. Most of these systems exhibit immiscibility or very limited solid solubility over a wide range of temperatures. Thus, bulk thermodynamics favors phase separation in the NPs and suppresses formation of homogeneous alloyed phase. However, capillary forces come into dominance at small sizes, and depending on the composition, size, and method of preparation, NPs are sometimes found in the homogeneous alloyed state as well<sup>17,19,20</sup>. In the same alloy system, variation of processing variables or exposure to moderately high temperatures can lead to the formation of thermodynamically more stable phase separated configurations.

For example, through a variation of process parameters of magnetron sputtering, Krishnan et al.<sup>17</sup> synthesized Cu-Mo NPs in a range of sizes (16-59 nm) and compositions (14-30 at.%Cu). They observed single phase, Cu@Mo<sup>2</sup> CS, and Janus morphologies in these NPs. They also reported an onion-like concentric ring configuration where a Cu middle ring was sandwiched between the outer shell and inner core made of Mo. This is surprising, because, based on surface energy considerations, an outer ring of Cu would have been more likely ( $\sigma_{\text{Cu}} < \sigma_{\text{Mo}}$ ,  $\sigma$  being the surface energy).

Exposure to high temperature too can lead to a change in the configuration. When Ag@Cu CS NPs of diameter  $\sim 25$  nm prepared by sequential chemical synthesis<sup>21</sup> were heated above 500 °C, the thin Ag shells ( $\sim 0.7$  nm thick) dewetted and produced Ag nodules on the surface of Cu cores. During continued heating, the NPs eventually coarsened to several hundred nanometers in size through coalescence. In contrast, when Cu-Ag NPs of near-equiatomic composition produced by pulsed laser deposition<sup>19</sup> were exposed to temperatures up to 600 °C, the initially homogeneous solid solution phase decomposed to form Ag- and Cu-rich phases. Figure 1, which is reproduced from this work<sup>19</sup>, shows that particles below  $\sim 20$  nm in size developed into a Janus configuration, while the larger ones (size  $\sim 40$  nm) exhibited an Ag@Cu CS morphology.

Radnoczi et al.<sup>20</sup> identified spinodal decomposition (SD) of the solid solution phase to be the underlying the mechanism of phase separation in Ag-Cu NPs prepared by DC magnetron sputtering. They found that irrespective of particle composition, there was no phase separation if the particle size was below a critical value (5 nm), and it matched well with the critical spinodal wavelength estimated using the Cahn-Hilliard (CH) theory<sup>22</sup>. They observed phase separation in larger Cu-rich NPs (30 at.%Ag) that resulted in the formation of Janus and off-centered Ag@Cu CS morphologies. Formation of other configurations such as ‘crescent’<sup>23,24</sup>, *i.e.*, side segregated with a curved interface between the two halves, and inverse CS<sup>13</sup> where the higher surface energy phase forms the shell, have also been reported.

Although experiments report a myriad of morphologies of BNPs as a function of processing, one requires to supple-

---

<sup>2</sup>we use A@B to refer to a CS configuration where A is the shell and B is the core

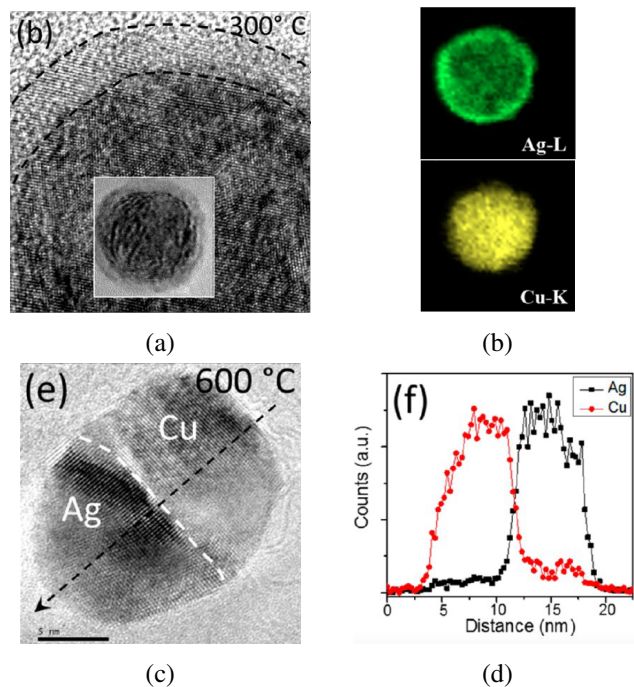


Figure 1 Core-shell and Janus structures of pulsed laser deposited near equiatomic Ag-Cu NPs as a function of particle size<sup>19</sup>: (a, b) high resolution transmission electron micrograph (HRTEM) of a 40 nm core-shell particle and the corresponding elemental composition map; (c, d) HRTEM of a 20 nm Janus particle and the corresponding elemental composition map. Reprinted with permission from Kirtiman Deo Malviya and K. Chattopadhyay, *Journal of Physical Chemistry C*, 2016, 120, 27699-27706. Copyright © 2016 American Chemical Society.

ment them with theoretical insights to understand the role of thermodynamic and kinetic factors leading to these structures. Computational studies aiming to understand the role of different factors influencing BNP configurations fall into two broad categories: (i) bulk and surface thermodynamics based models and (ii) electronic and atomistic simulations. The former essentially follows the CALPHAD approach<sup>25</sup>, but additionally incorporates finite-size corrections for surface energy into the Gibbs free energy description of the corresponding bulk alloy. This enables a re-assessment of thermal stability of nanoalloys and determination of phase diagrams as a function of particle size<sup>26-31</sup>. Although these models have been successful in predicting a shift in miscibility gap in nanoalloy systems, they do not provide sufficient insight into the internal morphological details of BNPs.

Electronic or atomistic models of nanoalloy clusters<sup>32-37</sup>, on the other hand, explore the relative stability of the different morphologies in BNPs using density functional theory, molecular dynamics or Monte Carlo (MC) simulations. Details of the extensive research carried out using these methods can be found in the monograph by Ferrando<sup>38</sup>. The primary goal of most, if not all, of these studies, however, is to predict the *equilibrium* or lowest energy configuration in specific systems as a function of particle size. A notable exception is the recent study by Li et al.<sup>39</sup> who performed kinetic MC simulations. It indicated the possibility of metastable, ‘kinetically trapped’ configurations due to partial redistribution of atoms in BNPs as small as 2 nm. Their study brought out the limitations of equilibrium studies which fail to account

for diffusion-limited processes. In particular, they show that the diffusion process becomes extremely sluggish after initial phase separation, leading to such metastable configurations.

Barring the last one, most studies have focused on equilibrium structures of BNPs. Although they reveal several important aspects of BNP morphology at equilibrium, one needs a systematic investigation of kinetic pathways leading to the formation of CS or Janus configurations. Such an investigation will be useful to identify the key mechanisms of evolution of these morphologies as a function of particle size, contact angle, alloy chemistry and other processing conditions.

Majority of the bimetallic systems constituting BNPs exhibit a miscibility gap in their bulk phase diagrams and their microstructures often consist of two compositionally-distinct, isostructural phases. This suggests spinodal to be a viable mechanism by which an initially homogeneous, alloyed BNP with equiatomic or near-equiatomic composition can phase separate and form CS/Janus structures<sup>9,19,20</sup>.

Although SD in bulk systems has been investigated extensively since Cahn<sup>22</sup>, there have been fewer studies on phase separation in confined geometries where external surfaces influence the decomposition. In a finite system, the constituent phase having a lower surface energy may prefer to form at the surface and trigger concentration waves propagating from surface to the interior. Compositionally modulated structures resulting from this surface-directed spinodal decomposition (SDSD) appear different from bulk spinodal morphology<sup>40,41</sup>.

In the past three decades, phase field models<sup>42</sup> have emerged as a very powerful continuum, mesoscale computational tool. They incorporate thermodynamics and kinetics of a system seamlessly, and are ideal for studying microstructures resulting from phase transformations such as SD. In addition to their extensive application in understanding bulk SD, they have also been used to study SD in finite systems such as thin films<sup>43,44</sup>, polycrystalline materials containing multiple internal surfaces<sup>45,46</sup>, systems containing inert dispersoids<sup>47</sup>, and isolated, radially-stressed spheres<sup>48</sup>.

Using a CH<sup>49</sup> formalism with an auxiliary non-conserved phase field variable<sup>50</sup>, we present a novel phase-field model of phase separation in confined systems. We report results of two-dimensional simulations using this model, and investigate morphological evolution driven by SD in an initially homogeneous, alloyed BNP. In particular, we address the following questions:

1. For a circular BNP of diameter  $d$ , how does the contact angle  $\theta$ , which represents the balance between surface and interfacial energies, influence the morphological evolution and final configuration?
2. For a given contact angle, how does the particle size influence the kinetic pathways and final morphology?

Further, we systematically explore the  $\theta - d$  space to study how both these factors interact, and summarize our findings through a morphology map. Finally, we also show how the shape of a BNP can be another important factor in determining



its internal morphology.

## 2 Model Formulation

When we study phase transformations in bulk systems, the governing CH equations employ periodic or zero-flux boundary conditions that arise naturally. However, since nanoparticles are finite systems by definition, we can no longer apply periodic boundary conditions, and zero-flux boundary conditions too fail to correctly incorporate the three-phase contact angle. Even the so-called ‘contact angle boundary condition’<sup>51,52</sup> is inappropriate and ill-imposed when contact angle develops dynamically, e.g., when an initial two-phase contact evolves to a three-phase contact or vice versa. As pointed out by Cahn in his pioneering work on ‘critical point wetting’, the equilibrium contact angle  $\theta$  cannot be defined<sup>53</sup> beyond complete wetting transition.

Thus, one of the critical challenges is to address the boundary condition in our problem. Immersed boundary (IB) method has emerged as an efficient technique in computational fluid dynamics to solve Navier-Stokes and other transport equations in complex geometries<sup>54</sup>. IB method uses an auxiliary function to capture irregular boundaries of a complex geometry inside a regular computational domain such that regular solvers can be employed without special meshing techniques. Bueno-Orovio et al.<sup>55</sup> implemented an IB technique in the Fourier space to solve partial differential equations in irregular geometries with zero-flux boundary conditions. They used a smoothly varying phase-field parameter to inscribe the physical region of interest in the extended computational domain. Li et al.<sup>56</sup> and Yu et al.<sup>57</sup> extended this method to include Dirichlet, Neumann and Robin boundary conditions. Poulsen and Voorhees<sup>58</sup> introduced an alternative energy-penalty based formulation which integrated IB with the variational phase-field framework. They demonstrated the efficacy of their technique by solving the heat diffusion problem during annealing.

We introduce a method similar in spirit to these smoothed IB techniques. However, since microstructural evolution inside a BNP can lead to a dynamical transition in the contact angle at the particle boundary, contact angle boundary condition on the particle surface cannot be imposed explicitly. As contact angle results from a balance of surface energies and interfacial energy at the particle surface, we implicitly incorporate it by first constructing an extended system containing a particle embedded in a matrix, and then choosing an appropriate free energy functional for the system. Through benchmark simulations, we demonstrate the capability of the model to successfully recover the correct contact angle.

Our model, shown schematically in Fig. 2, consists of an alloyed BNP immersed in an inert matrix phase  $\alpha$  that forms the surrounding environment of the particle. Chemically, it is a model binary system consisting of two atomic species A and B. When an initially homogeneous particle of composition  $c_0$  is brought below a critical temperature, it undergoes phase separation that leads to the formation of two isostructural terminal phases  $\beta_1$  and  $\beta_2$ . We use a non-conserved

order parameter field  $\phi(\mathbf{r})$  to distinguish the particle ( $\phi = 1$ ) from the matrix ( $\phi = 0$ ), and a conserved composition field  $c(\mathbf{r}, t)$  to describe phase separation within the particle. For numerical convenience, we scale  $c(\mathbf{r}, t)$  using the expression:  $c = (c' - c_{\beta_1}^{\text{eq}})/(c_{\beta_2}^{\text{eq}} - c_{\beta_1}^{\text{eq}})$  where  $c'$  denotes the unscaled composition variable, and  $c_{\beta_1}^{\text{eq}}, c_{\beta_2}^{\text{eq}}$  are the unscaled equilibrium compositions of  $\beta_1$  and  $\beta_2$ , respectively.

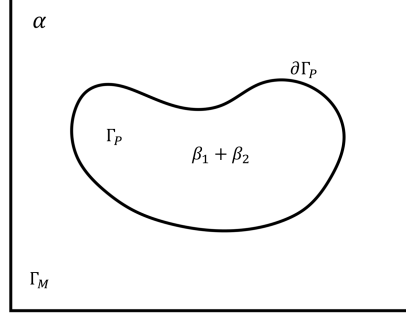


Figure 2 A spinodally decomposing particle of volume  $\Gamma_P$  embedded in a matrix of volume  $\Gamma_M$ .  $\Gamma = \Gamma_M \cup \Gamma_P$  is the volume of the entire domain.

## 2.1 Energetics

Three energy contributions (expressed in per atom basis) constitute the total free energy density of the phase-separating system:

1. The bulk *chemical* free energy density  $f_{\text{ch}}$ , which is the weighted average of the particle and the matrix free energies:  $f_{\text{ch}}(c, \phi) = h(\phi)f^\beta + (1 - h(\phi))f^\alpha$ , where  $f^\beta = f_0^p c^2(1 - c)^2$  is a double well potential denoting the particle free energy and  $f^\alpha = f_0^m (c - 0.5)^2$  is the free energy of the matrix. Here  $h(\phi) = \phi^3(10 - 15\phi + 6\phi^2)$  is a weighing function<sup>59</sup> varying smoothly between 0 and 1, and  $f_0^i (i = m, p)$  are temperature-dependent phenomenological constants that set the scale of free energy functions of the matrix and particle, respectively. This particular choice of  $f^\beta$  makes the scaled equilibrium  $\beta_1$  and  $\beta_2$  compositions 0 and 1, respectively. Without any loss of generality, we choose the minimum of the matrix free energy function at  $c = 0.5$  (midway between equilibrium compositions of  $\beta_1$  and  $\beta_2$ ) describing a three-phase equilibrium between the matrix ( $\alpha$ ) and the particle ( $\beta_1$  and  $\beta_2$ ). The equilibrium values of  $c$  and  $\phi$  in different phases are summarized in Table 1.

Note that the double-well potential  $f^\beta$  used in our model can be compared to the regular solution potential through the relation  $\frac{f^\beta}{k_B T} = \Omega c(1 - c) + c \ln c + (1 - c) \ln(1 - c)$  where  $k_B$  is Boltzmann constant,  $T$  is temperature in kelvin, and  $\Omega$  is the regular solution parameter normalized with  $k_B T$ . Free energy barrier heights in these two potentials at equiatomic composition are related by  $\frac{f_0^p}{16k_B T} = \Omega/4 - \ln 2$ .

2. A double-well free energy function  $f_{\text{br}}$  that introduces a potential *barrier* between the particle and the matrix:  $f_{\text{br}}(c, \phi) = \omega(c)\phi^2(1 - \phi)^2$ , where the composition-dependent variable  $\omega(c)$  sets the scale for the barrier. We

choose  $\omega(c) = \omega_0(1 - \chi c)$  where  $\chi$  is a parameter that governs solute segregation to the particle-matrix interface, similar to the one used by Ågren and coworkers<sup>60</sup> to study solute drag effects on grain boundary migration.

3. A gradient energy contribution  $f_{\text{gr}}$  that accounts for the surface excess associated with the matrix-particle interface as well as interfaces between  $\beta_1$  and  $\beta_2$  phases:  $f_{\text{gr}} = \kappa_\phi |\nabla\phi|^2 + \kappa_c |\nabla c|^2$ , where  $\kappa_\phi$  and  $\kappa_c$  are the positive gradient energy coefficients associated with composition and phase field variables, respectively. For a given alloy particle,  $\kappa_c$  controls the length scale of SD leading to CS/Janus structures.

The total free energy functional of the system,  $\mathcal{F}$ , is given as:

$$\mathcal{F} = N_v \int_{\Gamma} (f_{\text{ch}} + f_{\text{br}} + f_{\text{gr}}) d\Gamma, \quad (1)$$

where  $N_v$  denotes number of atoms per unit volume. Since we use  $\phi$  only as an auxiliary parameter to distinguish the particle from the matrix, any continuous  $\phi$  profile that satisfies  $\phi = 0$  and  $\phi = 1$  for matrix and particle, respectively, would suffice. We have chosen a smooth tanh function for the variation of  $\phi$  across the particle-matrix interface:

$$\phi(\mathbf{r}) = \frac{1}{2} \left[ 1 - \tanh \left( \frac{|\mathbf{r}| - (d/2)}{W_\phi} \right) \right]. \quad (2)$$

Here  $W_\phi$  sets the width of the matrix-particle interface (kept constant for all our simulations),  $|\mathbf{r}|$  is the magnitude of the position vector measured from the centre of the particle, and  $d$  is the particle diameter. Alternatively, one could additionally solve Allen-Cahn equation<sup>50</sup> for  $\phi$  for a specified number of time steps to achieve regularization of matrix-particle interface of any arbitrary geometry. For the chosen  $\phi$  profile, we obtain the equilibrium composition profile  $c^{\text{eq}}(\mathbf{r})$  by solving the Euler-Lagrange equation for the variational problem:

$$\frac{\delta \mathcal{F}}{\delta c} = \frac{\partial f}{\partial c} - 2\kappa_c \nabla^2 c = 0. \quad (3)$$

Using the  $c^{\text{eq}}(\mathbf{r})$  profile between any two of  $\alpha$ ,  $\beta_1$  and  $\beta_2$  phases at a time, we compute the corresponding interfacial

**Table 1** Equilibrium values of  $c$  and  $\phi$  for all the phases

Phase	$c^{\text{eq}}$	$\phi^{\text{eq}}$
$\beta_1$	0	1
$\beta_2$	1	1
$\alpha$	0.5	0

energy  $\sigma$  as:

$$\sigma = \int_{-\infty}^{\infty} (\Delta f(c^{\text{eq}}, \phi) + \kappa_c |\nabla c^{\text{eq}}|^2 + \kappa_\phi |\nabla \phi|^2) d\Gamma. \quad (4)$$

Here,  $\Delta f(c^{\text{eq}}, \phi) = f(c^{\text{eq}}, \phi) - (1-c)\mu_A^{\text{eq}} - c\mu_B^{\text{eq}}$ , where  $\mu_{A/B}^{\text{eq}}$  denotes the chemical potential of the corresponding species. In what follows,  $\sigma_1$  and  $\sigma_2$  refer to the energies of  $\alpha$ - $\beta_1$  and  $\alpha$ - $\beta_2$  interfaces (the ‘surface energies’), respectively, while  $\sigma_{12}$  denotes the  $\beta_1$ - $\beta_2$  interfacial energy.

The segregation parameter  $\chi$  modifies the free energy landscape in regions of non-uniform  $\phi$  (*viz.*, within the matrix-particle interface). In doing so, a non-zero  $\chi$  makes  $\alpha$ - $\beta_1$  and  $\alpha$ - $\beta_2$  interfaces non-equivalent, which is illustrated in Fig. 3 using surface and contour plots of  $f_{ch} + f_{br}$  in the  $c$ - $\phi$  space. While the free energy is perfectly symmetric about  $c = 0.5$  in Fig. 3a ( $\chi = 0$ ), it becomes increasingly more asymmetric as  $\chi$  continues to increase in Fig. 3b through Fig. 3d. This asymmetry is revealed most strikingly in Fig. 3e through the free energy – composition ( $f$ - $c$ ) curves drawn at  $\phi = 0.5$ . In this figure,  $f(c, 0.5)$  is symmetric about  $c = 0.5$  for  $\chi = 0$ , but non-zero  $\chi$ 's create asymmetry by shifting the minimum of  $f$  towards right. Figs. 3f and 3g present the  $f$ - $c$  curves corresponding to matrix ( $\phi = 0$ ) and particle ( $\phi = 1$ ), respectively. The free energy function for the matrix has a single minimum, whereas that for the particle is a double-well potential corresponding to the two equilibrium phases  $\beta_1$  and  $\beta_2$ .

Since the choice of  $\chi$  influences interface profiles and thereby energies associated with the interfaces, it provides us a useful means to tailor the surface energies of the  $\beta_1$  and  $\beta_2$  phases. Young's equation for the contact angle  $\theta$  at a three-phase coexistence point connects these surface energies and the  $\beta_1$ - $\beta_2$  interfacial energy:

$$\cos \theta = \frac{\sigma_1 - \sigma_2}{\sigma_{12}}. \quad (5)$$

Hence, we use  $\chi$  as a parameter to systematically vary the contact angle and study how the balance between surface and interfacial energies influences the morphological evolution in BNPs. As an extension to Young's equation, Cahn has discussed the condition for spontaneous or complete wetting<sup>53</sup> when the following condition is satisfied:

$$\sigma_1 \geq \sigma_2 + \sigma_{12}. \quad (6)$$

In this case, the lower surface energy phase  $\beta_2$  perfectly wets the high-energy  $\alpha$ - $\beta_1$  interface and replaces it with two low-energy interfaces, *viz.*,  $\alpha$ - $\beta_2$  and  $\beta_1$ - $\beta_2$ . The inequality condition in Eq. (6) sets the limit of applicability of Eq. (5). Note that the chosen values of  $\chi$  for BNP simulations result in a variation of the contact angle  $\theta$  from  $90^\circ$  to  $0^\circ$ .

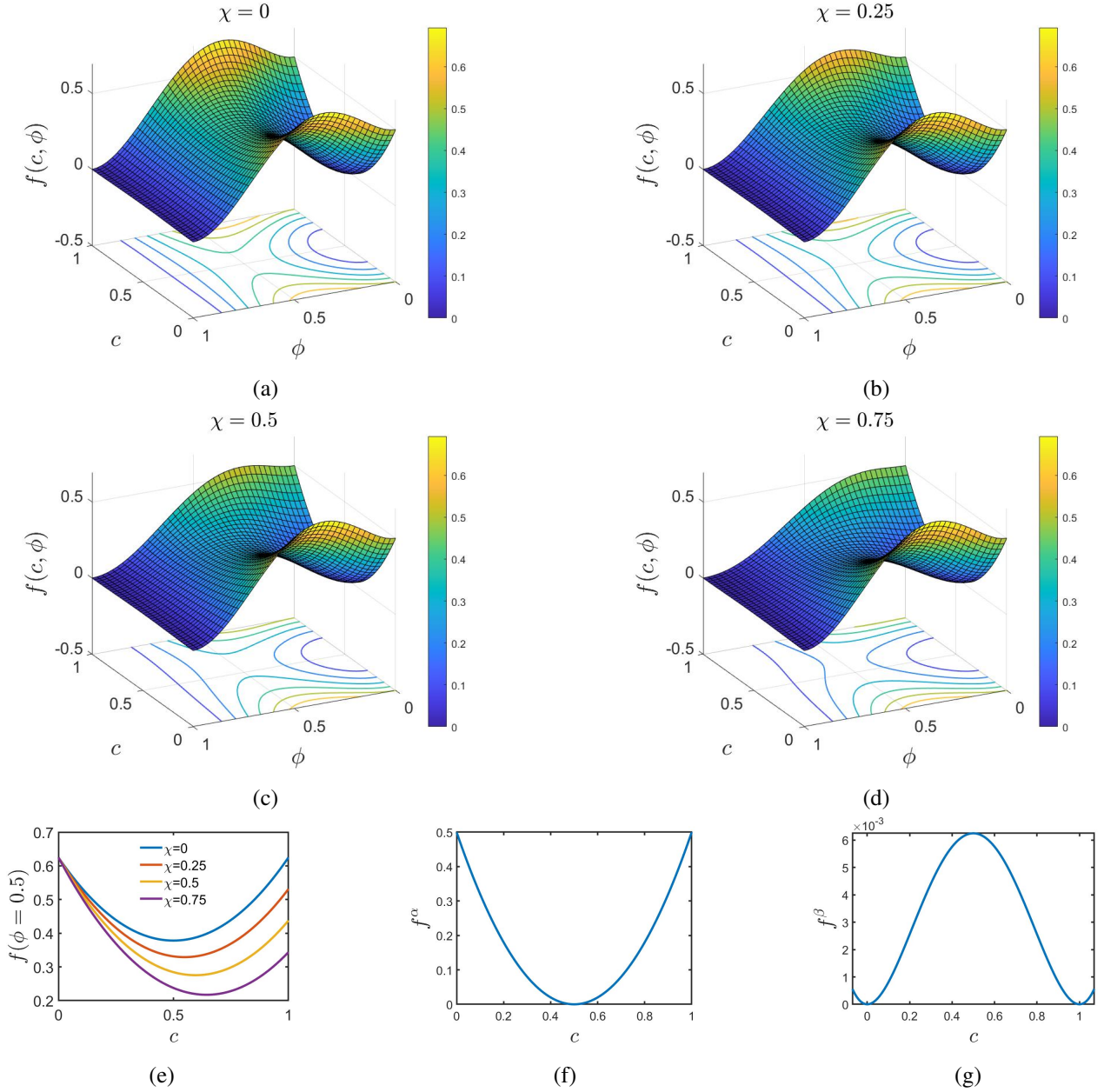


Figure 3 Free energy density ( $f_{ch} + f_{br}$ ) of the matrix-particle system as a function of  $c$  and  $\phi$ . (a–d): Surface plots along with iso-energy contours for different values of the segregation parameter  $\chi$ . (e) Free energy-composition curves drawn at  $\phi = 0.5$  for different values of  $\chi$ . (f–g): Bulk free energy-composition curves of the matrix ( $\phi = 0$ ) and particle ( $\phi = 1$ ), respectively; only one curve suffices as  $\chi$  does not affect free energy of bulk regions.

## 2.2 Kinetics

In our simulations, a BNP is initially in the homogeneous alloyed configuration. However, this state is thermodynamically unstable, and it undergoes phase separation by SD. Phase separation and subsequent establishment of the proper three-phase equilibrium at the particle surface are achieved by solute transport inside the BNP. Cahn-Hilliard equation<sup>22</sup>, which describes the evolution of composition field over time, governs the kinetics of solute transport in the system:

$$\begin{aligned}\frac{\partial c}{\partial t} &= \nabla \cdot M(\mathbf{r}) \nabla \mu \\ &= \nabla \cdot M(\mathbf{r}) \nabla \left( \frac{\partial f}{\partial c} - 2\kappa_c \nabla^2 c \right),\end{aligned}\quad (7)$$

where  $\mu \equiv \frac{\delta \mathcal{F}}{\delta c} = \partial f / \partial c - 2\kappa_c \nabla^2 c$  is the generalized diffusion potential.  $M(\mathbf{r}) = M_c \phi$  defines the position-dependent atomic mobility of the solute,  $M_c$  being the constant solute mobility within the particle ( $\phi = 1$ ). This functional form of  $M(\mathbf{r})$  ensures that no diffusion takes place in the matrix and diffusional mobility is constant within the particle. Thus, SD and wetting dynamics are controlled solely by diffusion within the particle and precludes interactions with neighbouring particles due to periodic computational domain  $\Gamma$ . Although here we do not report the effects of matrix diffusion or coalescence of particles on wetting, our formulation is general enough to include such effects through an appropriate choice of  $M(\mathbf{r})$ . We nondimensionalize all parameters in the governing equation (Eq. (7)) using a characteristic energy  $E_c = k_B T$ , a characteristic length  $L_c = (\kappa_c / k_B T)^{1/2}$ , and a characteristic time  $\tau_c = L_c^2 / M_c E_c$ . Nondimensional values of all physical and numerical parameters used in the simulations are listed in Table 2.

We solve Eq. (7) numerically in the extended computational domain  $\Gamma$  using a semi-implicit Fourier spectral method<sup>61</sup>. An operator splitting approach using a constant weighing parameter  $Q$  ( $0 \leq Q \leq 1$ ) introduces implicitness to the linear terms in the discretized equation in the reciprocal space and thereby reduces the computational time<sup>62</sup>:

$$\tilde{c}^{n+1} = \frac{\tilde{c}^n (1 + 2Q\kappa_c k^4 \Delta t) + \mathbf{i} \mathbf{k} \Delta t \cdot \{ M \phi(\mathbf{r}) ([\mathbf{i} \mathbf{k}' \tilde{\mu}]_{\mathbf{k}'}^n)_{\mathbf{r}} \}_{\mathbf{k}}}{1 + 2Q\kappa_c k^4 \Delta t}.\quad (8)$$

Here  $\mathbf{k}$  is the reciprocal (Fourier) space vector and  $k = |\mathbf{k}|$  denotes its magnitude,  $\{\tilde{\cdot}\}$  over a field variable represents it in the Fourier space,  $\{\cdot\}_{\mathbf{k}}$  or  $[\cdot]_{\mathbf{k}'}$  denotes Fourier transform of the quantity inside the brackets,  $(\cdot)_{\mathbf{r}}$  represents the inverse Fourier transform,  $\mathbf{i} = \sqrt{-1}$ ,  $\Delta t$  is and the value of a discrete time step, and superscripts  $n$  and  $n + 1$  denote the current and next time-steps, respectively. We use the forward Euler method to advance the composition field in time, and carry out a sensitivity analysis to choose an appropriately small time step that ensures temporal stability and accuracy.

The discretized equation (Eq. 8) is solved on a Xeon Phi vector processor with 72 CPU cores using OpenMP parallelization or an NVIDIA Tesla V100 GPU card having 5120 cores. The Fourier transforms are implemented using the open source `fftw`<sup>63</sup> or NVIDIA `cufft` library. We systematically investigate the effects of contact angle and particle size on SD and wetting behaviour of an isolated, circular NP embedded in an inert matrix. The simulations are run till equilibrium, measured computationally by comparing the largest difference in chemical potential of the system between successive steps with a tolerance of  $10^{-10}$ .

**Table 2** Simulation Parameters

Parameter	Value
Average particle composition $c_0$	0.5
Number density of atoms $N_v$	0.37
Matrix free energy coefficient $f_0^m$	2
Particle free energy coefficient $f_0^p$	0.1
Barrier height $\omega_0$	6
Gradient energy coefficient $\kappa_c$	1
Gradient energy coefficient $\kappa_\phi$	15
Segregation parameter $\chi$	0.0, 0.25, 0.5, 0.75
Solute mobility in particle $M_c$	1.0
Grid size $\Delta x, \Delta y$	1.0, 1.0
Time step $\Delta t$	0.1
Particle size $d$	140, 160, 180, 240
Amplitude of initial noise $\eta$	1%

### 3 Results and Discussion

We first discuss the role of the parameter  $\chi$  on solute segregation at the particle surface and consequently on surface energies. Through a series of drop-on-substrate simulations, we demonstrate how  $\chi$  can be used to systematically vary the three-phase ( $\alpha$ - $\beta_1$ - $\beta_2$ ) contact angle  $\theta$ . Following this, we present simulations of phase-separating particles embedded in a matrix as a function of their size and the contact angle, and discuss underlying mechanisms for the morphological evolution. These are summarized through a morphology map for CS and Janus configurations. Finally, through simulations of elliptical BNPs, we illustrate how the shape of the NPs can influence morphological evolution and even give rise to novel configurations.

#### 3.1 Surface segregation, surface energy and contact angle

In our model, the parameter  $\chi$  controls solute segregation at the particle surface, and consequently, influences the surface energies of the phases. To compute interfacial energies between different phases using Eq. 4, we first obtain equilibrium composition profiles across them by carrying out one-dimensional (1D) simulations. Figs. 4(a–d) present these profiles across the  $\alpha$ - $\beta_1$  interface for different values of  $\chi$ . These profiles have peaks in solute concentration within the interface region, and the peak compositions increase with increasing  $\chi$ . The profiles for the  $\alpha$ - $\beta_2$  interface shown in Figs. 4(e–h),

on the other hand, do not exhibit any intermediate peak, but increased  $\chi$  appears to reduce the width of the compositional interface. The composition profile for the  $\beta_1$ - $\beta_2$  interface remains completely unaffected by  $\chi$  and is not presented here.

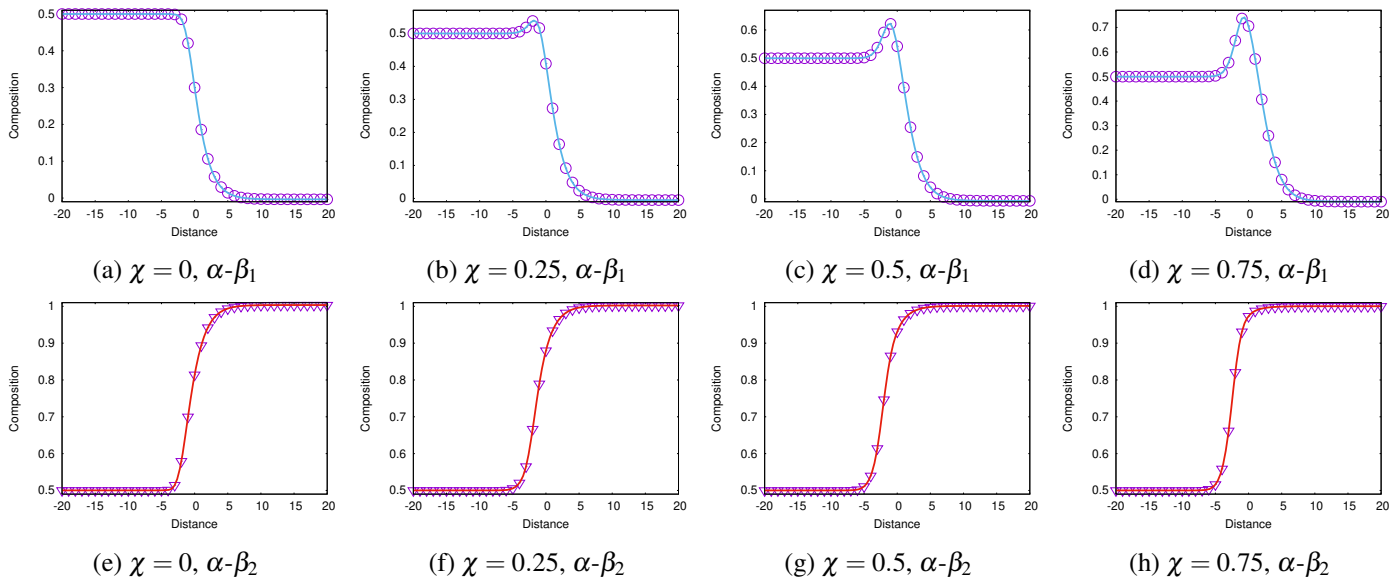


Figure 4 Equilibrium composition profiles across  $\alpha\text{-}\beta_1$  (top row) and  $\alpha\text{-}\beta_2$  (bottom row) interfaces for (a, e)  $\chi = 0$ , (b, f)  $\chi = 0.25$ , (c, g)  $\chi = 0.5$ , (d, h)  $\chi = 0.75$

Table 3 lists interfacial energies computed from the equilibrium composition profiles and corresponding contact angles estimated using Eq. (5).

**Table 3** Variation of interfacial energies and contact angle with  $\chi$

$\chi$	$\sigma_1$	$\sigma_2$	$\sigma_{12}$	$\theta$
0	3.31	3.31	0.11	90°
0.25	3.07	3.03	0.11	69°
0.5	2.80	2.72	0.11	43°
0.75	2.50	2.39	0.11	0°

Fig. 5 shows that the equilibrium solute segregation at the high-energy  $\alpha\text{-}\beta_1$  interface increases with increasing  $\chi$ . The extent of segregation is represented here by the maximum in interface composition,  $C_{\text{mx}}$ , as revealed in Fig. 4. We note that  $C_{\text{mx}}$  is similar to the limiting surface composition  $C_s$  defined by Cahn in his theory of wetting<sup>53</sup>; however, a direct correspondence is not possible as  $C_s$  cannot be obtained analytically.

Fig. 5 also shows that the three-phase contact angle  $\theta$  decreases with increasing  $\chi$ . Although surface energies of both  $\beta_1$  and  $\beta_2$  phases decrease with increasing  $\chi$ , the reduction in  $\sigma_2$  is greater than that of  $\sigma_1$  (see Table 3). This is a direct consequence of the way  $\chi$  affects the  $f\text{-}c$  curves of Fig. 3e: free energy function becomes more asymmetric with increasing  $\chi$ , dropping to increasingly lower levels at the  $\beta_2$  end ( $c = 1$ ). Moreover, a comparison of equilibrium  $\alpha\text{-}\beta_2$  profiles reveals lower gradient energy contributions as  $\chi$  increases (see the bottom row of Fig. 4). Huang *et al.* have discussed a similar asymmetry in the context of interfacial adsorption in ternary alloys<sup>64</sup>. Thus increasing  $\chi$  results in a



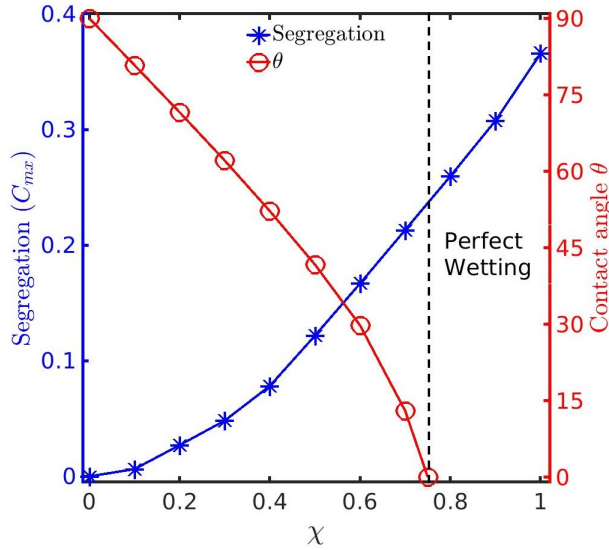


Figure 5 Variation of equilibrium segregation and contact angle with  $\chi$

monotonic increase of the difference between the surface energies,  $\Delta\sigma = \sigma_1 - \sigma_2$ , which leads to a corresponding decrease in contact angle  $\theta$ . At  $\chi = 0.75$ ,  $\theta$  becomes zero; any further increase in  $\chi$  continues to increase the segregation, but no contact angle can be defined under this perfect wetting regime as the low-energy  $\alpha$ - $\beta_2$  interface completely replaces the three-phase contact.

We note that there may be challenges in determining  $\chi$  accurately from first-principles calculations or experiments. Experimental measurements of surface segregation in alloy nanoparticles<sup>31,65,66</sup> can be a viable route to determine  $\chi$  if a proper correlation between surface energy and extent of segregation can be established. Atomistic simulations of alloy nanocrystals that account for interactions between the alloy constituents with the surrounding medium can also give useful insights on the surface segregation and its role on the stability of nanocrystals<sup>31,65,67-69</sup>.

### 3.2 Drop-on-substrate simulations

The contact angle can play a crucial role during phase separation in confined geometries. In some recent phase field models<sup>57,70</sup>, it has been imposed as a boundary condition over the confined domain. Our model, however, does not require imposition of any additional condition or constraint: the correct contact angle is recovered naturally for the chosen set of relevant free energy parameters (*viz.*,  $f_0^m, f_0^p, \omega_0, \kappa_c, \kappa_\phi$ , and  $\chi$ ).

Fig. 6 demonstrates the capability of our model in capturing wetting behavior with the correct contact angle. We choose a drop-on-substrate configuration where we initially place a  $\beta_2$  droplet (blue) on an  $\alpha$  (grey) substrate;  $\beta_1$  phase (white) surrounds the droplet, thereby creating two three-phase contact points. The droplet evolves via diffusion along the interfaces till the three-phase contact angle attains equilibrium. To have both acute and obtuse contact angles in these simulations, we have chosen positive and negative values of  $\chi$ , respectively. For a given size, the initial shape of the drop

does not influence the kinetic path to the final configuration. The contact angles measured on the final configurations using level sets for  $c$  and  $\phi$  at 0.5 agree with those predicted by Young’s equation within  $\pm 2^\circ$  (Table 3).

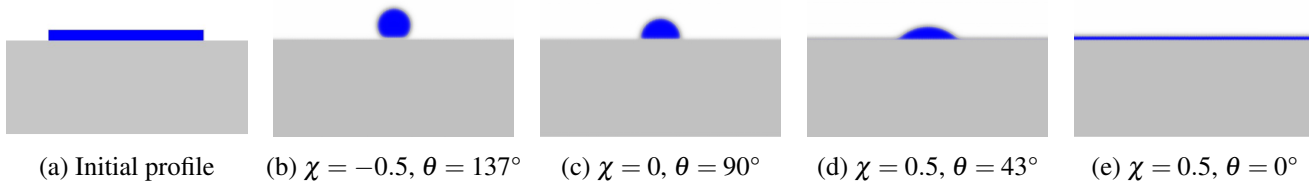


Figure 6 Attainment of correct contact angle of a drop on a substrate: (a) initial drop (b-e) final configurations for different values of  $\chi$

### 3.3 Morphology as a function of size and contact angle

BNPs primarily exhibit two distinct types of morphology: CS and Janus<sup>1</sup>. In addition to contact angle, factors such as particle size and shape, and alloy composition too can influence the morphology. Since one of our major goals is to understand the role of surface energies on SD-induced transformations in confined domains, we focus mainly on circular particles which have a constant curvature at the surface. Such a configuration permits a fundamental investigation of the effect of size on wetting/dewetting dynamics without complexities arising from curvature gradients in non-circular particles.

We first present the evolution of domains inside an isolated, initially homogeneous BNP of equiatomic composition which has been quenched from a high temperature to a temperature below the critical point of the miscibility gap. Figs. 7–9 present time snapshots corresponding to the early, intermediate and late stages of its evolution, respectively. In all these figures,  $\chi$  increases (and  $\theta$  decreases) from left to right, and particle size increases from top to bottom. The solute-rich  $\beta_2$  and solute-poor  $\beta_1$  phases in the particle are represented by blue and green colors, respectively; matrix is colored white to render it invisible. Animations of the evolution process for representative cases are available in the Electronic Supplementary Information (ESI).

Simulations with  $\chi = 0$  (*i.e.*,  $\theta = 90^\circ$ ) exhibit similar morphological evolution at all times irrespective of particle size and it finally leads to a straight Janus morphology with a 2-fold symmetry about the center of the particle (see the first column of Fig 9). First column of Fig. 7 shows that in this case, SD initiates homogeneously within the bulk of the particle with no apparent preference for the surface. During later times (first column of Fig. 8), coarsening sets in, and eventually  $\beta_1$ - $\beta_2$  interface makes a  $90^\circ$  contact angle at the particle surface (first column of Fig. 9), as is expected from Young’s equation (Eq. (5)). Absence of solute segregation in the equilibrium composition profiles in Fig. 4(a) implies a surface-agnostic evolution in this case ( $\chi = 0$  or  $\theta = 90^\circ$ ).

<sup>1</sup>Although some other forms such as “onion-like”, “dumbbell”, “ball and cup” morphologies have been reported<sup>1,65,71–75</sup>, these are mostly intermediate forms of CS and Janus structures (see, for example, Fig. 7 for an “onion-like” layered structure)

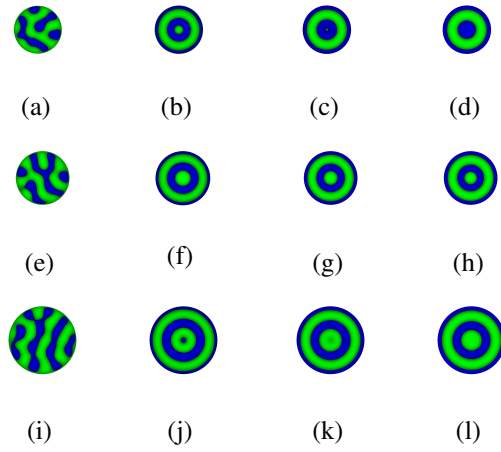


Figure 7 Early-stage time snapshots of evolution of BNP morphology. First, second, third and fourth columns correspond to  $\chi = 0$ ,  $\chi = 0.25$ ,  $\chi = 0.5$ , and  $\chi = 0.75$ , respectively. Particle size  $d$  in the top, middle, and bottom row is 140, 160, and 180, respectively; simulation boxes are scaled accordingly to reflect relative sizes. Blue and green colors represent solute-rich  $\beta_2$  and solute-poor  $\beta_1$  phases, respectively.

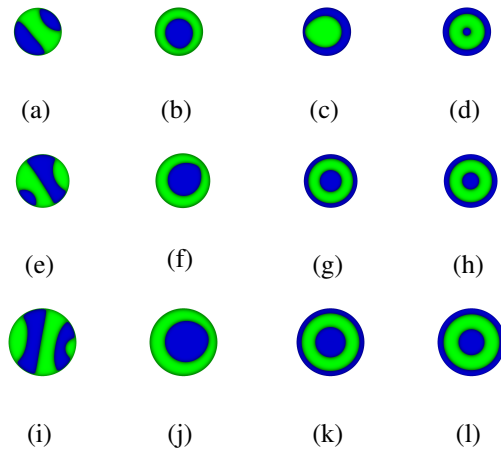


Figure 8 Intermediate-stage time snapshots of evolution of BNP morphology. First, second, third and fourth columns correspond to  $\chi = 0$ ,  $\chi = 0.25$ ,  $\chi = 0.5$ , and  $\chi = 0.75$ , respectively. Particle size  $d$  in the top, middle, and bottom row is 140, 160, and 180, respectively; simulation boxes are scaled accordingly to reflect relative sizes. Blue and green colors represent solute-rich  $\beta_2$  and solute-poor  $\beta_1$  phases, respectively.

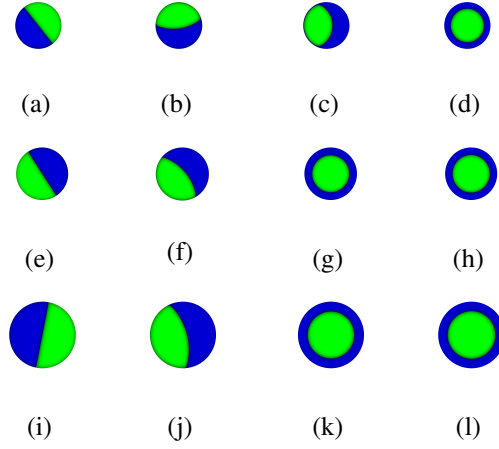


Figure 9 Final time snapshots of evolution of BNP morphology. First, second, third and fourth columns correspond to  $\chi = 0$ ,  $\chi = 0.25$ ,  $\chi = 0.5$ , and  $\chi = 0.75$ , respectively. Particle size  $d$  in the top, middle, and bottom row is 140, 160, and 180, respectively; simulation boxes are scaled accordingly to reflect relative sizes. Blue and green colors represent solute-rich  $\beta_2$  and solute-poor  $\beta_1$  phases, respectively.

When  $0 < \chi \leq 0.75$  ( $90^\circ > \theta \geq 0^\circ$ ), early stages of evolution at all particle sizes lead to solute segregation at the surface. Consequently, alternate solute-rich and solute-poor rings form due to SDS. Subsequent coarsening of the rings due to capillarity leads to an intermediate CS morphology, either with a solute-rich  $\beta_2$  shell and a solute-poor  $\beta_1$  core, or a solute-poor  $\beta_1$  shell and a solute-rich  $\beta_2$  core – we call them CS-2@1 and CS-1@2, respectively, where ‘1@2’ implies  $\beta_1$  shell on  $\beta_2$  core and vice versa.

The circular core in these cases starts to become distorted at later times for certain combinations of particle size and  $\theta$ . Specifically, we can observe this in Figs. 8(b, c, f, j) where the core undergoes a symmetry-breaking shape transition to an oval with its sharper end coming in close proximity to the particle surface. This sets up a diffusion field along the  $\beta_1$ - $\beta_2$  interface which leads to the breakdown of the intermediate CS structure and eventual formation of a Janus structure. In the very late stages, the contact angle formed by the Janus configuration approaches the corresponding equilibrium value, as shown in Figs. 9(b, c, f, j). Although our simulations provide discrete combinations of size and contact angle that exhibit these CS→Janus transitions, these are likely to take place within broader window of the  $d$ - $\theta$  continua.

When perfect wetting condition is satisfied ( $\theta = 0^\circ$ ), last columns of Figs. 7–9), decomposition proceeds with spontaneous solute enrichment of the particle surface which increases with time until the surface concentration reaches that of equilibrium  $\beta_2$ . In this case, the end product of coarsening is always CS-2@1, in accordance with the Cahn wetting condition, Eq. (6). Interestingly, we observe spontaneous enrichment of solute even when wetting is imperfect (*e.g.*,  $\chi = 0.5$ ). For small enough contact angles, the difference between the surface energies,  $\Delta\sigma$ , is large, and CS→Janus transition is arrested, especially at larger particle sizes. As a result, CS-2@1 configuration remains stable (see, *e.g.*, Figs. 9(g, k)).

In addition to CS-2@1 and Janus, there is yet another final configuration possible at larger particle sizes. When

$0 < \chi < 0.75$  and  $d > 180$ , solute redistribution following SDSA leads to a CS-1@2 structure where the phase having a larger surface energy ( $\beta_1$ ) forms the shell. Fig. 10 shows the morphological evolution in particles of size  $d = 240$  for  $\chi = 0.25$  and  $0.5$  (corresponding animations are provided in ESI). Initial layered structure formed by SDSA in these larger particles is similar to what is observed in smaller particles (see second column of Fig. 7 for comparison), although the number of rings is greater in the larger particle. Unlike in smaller particles, however, the core does not destabilize in the larger particle at later times, and the outermost solute-poor layer (green) continues to widen, resulting in the final CS-1@2 morphology. Note that when the phase with a higher surface energy - here solute-poor  $\beta_1$  - forms the shell, its outer surface is always enriched with solute, as indicated by the  $C_{mx}$  values in the top row of Fig. 4 corresponding to  $\alpha$ - $\beta_1$  interface. The likelihood of ending up with this morphology increases with increasing particle size, except for  $\chi = 0.75$  (*i.e.*,  $\theta = 0^\circ$ ) which always forms CS-2@1 morphology.

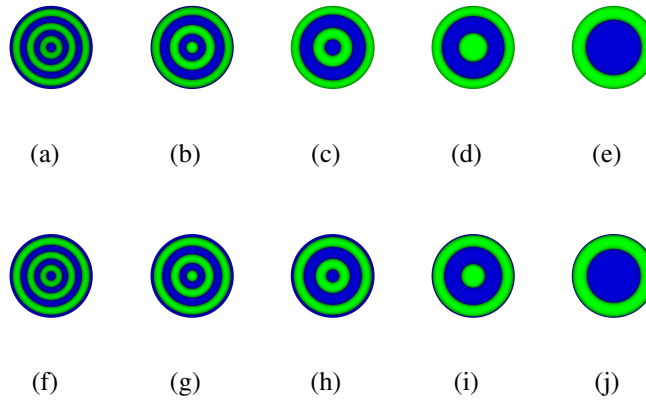


Figure 10 Time snapshots of microstructural evolution within a circular particle of size  $d = 240$  showing various stages of evolution. Top row (a-e):  $\chi = 0.25$ , bottom row (f-j):  $\chi = 0.5$ . Time increases from left to right in a row. Blue and green colors represent solute-rich  $\beta_2$  and solute-poor  $\beta_1$  phases, respectively.

### 3.4 Mechanisms of morphological evolution

As mentioned earlier, various studies have reported a wide spectrum of BNP configurations, CS and Janus being the two most frequently observed ones. Although most of these studies have focused on the final morphology and not how it is attained, some mechanisms have been put forward or speculated as possible means to achieve CS and Janus configurations. These include coalescence of individual NPs<sup>6,76-78</sup>, thin film dewetting and re-solidification<sup>79</sup>, or strain effects arising from the size mismatch of the constituent atoms<sup>32,35,80,81</sup>. Simulations presented here establish another route, *viz.*, SD of homogeneous alloyed BNPs, by which these structures can form. Incidentally, this appears to be the operative mechanism in BNPs synthesized using solvothermal co-reduction<sup>9</sup>, pulsed laser ablation<sup>19</sup> or sputtering<sup>20,82</sup>.

Our simulations show that when segregation is absent ( $\chi = 0$ , Fig. 4a), evolution proceeds with bulk phase separation. It eventually leads to an ideal Janus structure where the two halves of the particle are separated by a flat interface along a diameter (for example Fig. 9a). In the presence of segregation ( $\chi \neq 0$ ), there are two possible pathways to reach a Janus

morphology. The first one involves heterogeneous nucleation of one of the phases on the surface of a supersaturated alloy particle, and its subsequent growth leads to a ‘side-segregated’ morphology<sup>6,19</sup>. Alternatively, Janus structures can form through a three-step process: (i) initially, SDS produces an onion-like morphology comprising of alternate rings, (ii) these rings coarsen to form a CS morphology, and finally, (iii) the CS structure is destabilized by interface-induced disturbances and small fluctuations present in the system to form a Janus.

Heterogeneous nucleation mechanism requires composition waves that are *large in degree, but small in extent*<sup>22</sup>. To investigate this mechanism, one requires to introduce large, sustained fluctuations. The current study, on the other hand, deals with systems having a miscibility gap which permits spontaneous phase separation. It can occur with small initial fluctuations or even without it. Most of the systems constituting BNPs have miscibility gaps, which makes SD the more likely mechanism adopted by the system to form Janus.

Disruption of intermediate CS structure produced by SDS proceeds through core destabilization and subsequent core movement towards the surface of the particle. Core destabilization initiates through a breakdown of the circular symmetry of the radial composition profiles due to interface induced disturbances. For example, Fig. 11a presents an intermediate-time composition profile taken along a diameter of a particle shown in Fig. 8f ( $d = 160$ ,  $\chi = 0.25$ ): this plot clearly illustrates the breaking down of the symmetry of the composition ‘line scan’ with respect to the center of the particle. In contrast, the profile presented in Fig. 11b for the same particle size but with a higher  $\chi$  (Fig. 8g) retains its symmetry. Consequently, the particle with a lower  $\chi$  (*i.e.*, higher  $\theta$ ) undergoes core distortion, which evolves from a circle to an oval, and it finally results in a Janus configuration; the particle with a higher  $\chi$  (lower  $\theta$ ), however, retains the symmetric CS structure. Animations depicting the morphological evolution for both the cases are provided as ESI.

Core destabilization depends on the contact angle ( $\theta$ ) as well as particle size ( $d$ ). For systems closer to the perfect wetting condition (*i.e.*, smaller  $\theta$ ’s), radial composition profiles have a stronger tendency to retain their circular symmetry and prefer a CS structure. However, for a given contact angle  $\theta$ , circular rings are more unstable in smaller particles as their relatively large higher surface area to volume ratio makes them more susceptible to interface-induced disturbances.

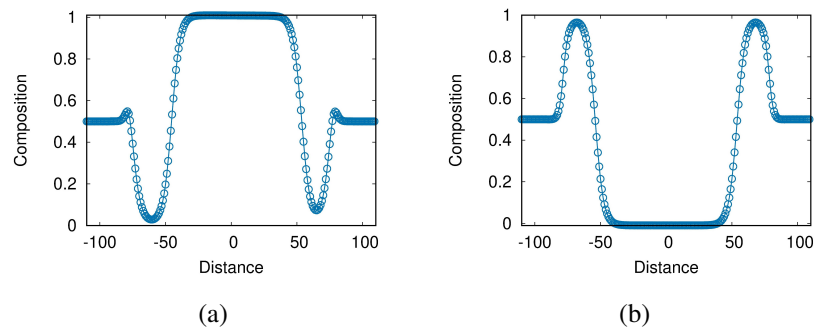


Figure 11 Composition profiles along a diameter of a particle with  $d = 160$  for (a)  $\chi = 0.25$  and (b)  $\chi = 0.5$  highlighting the breakdown and retention, respectively, of circular symmetry in these two cases.

Surface solute segregation plays an important role in events leading up to the formation of CS as the final configuration in certain systems. Formation of a segregated layer initiates SDSD with radial composition waves propagating from surface of the particle towards its center. For systems with a larger  $\chi$  and relatively smaller  $d$ , transformation proceeds by spontaneous and monotonic solute enrichment of the segregated layer by the spinodal mechanism. The maximally growing wavelength of the composition waves formed by this mechanism is dictated by the greater of the surface energies. It results in an outermost  $\beta_2$  ring that grows inward, leading to a CS-2@1 structure.

We present evolution of the radial composition profiles for two such systems with  $d = 160$  in Fig. 12(a) and (b) for  $\chi = 0.75$  and  $0.5$ , respectively. The upward pointing arrow in these figures represent a monotonically increasing solute enrichment at the matrix-particle interface. In contrast, for systems with a lower  $\chi$  and/or at larger sizes, the initial solute enrichment at the surface is followed by a decay, eventually settling to an equilibrium segregation value  $C_{mx}$ . Figs. 12c-d show this non-monotonic evolution (indicated by the up-and-down arrows) of surface composition for two different combinations of  $d$  and  $\chi$ .

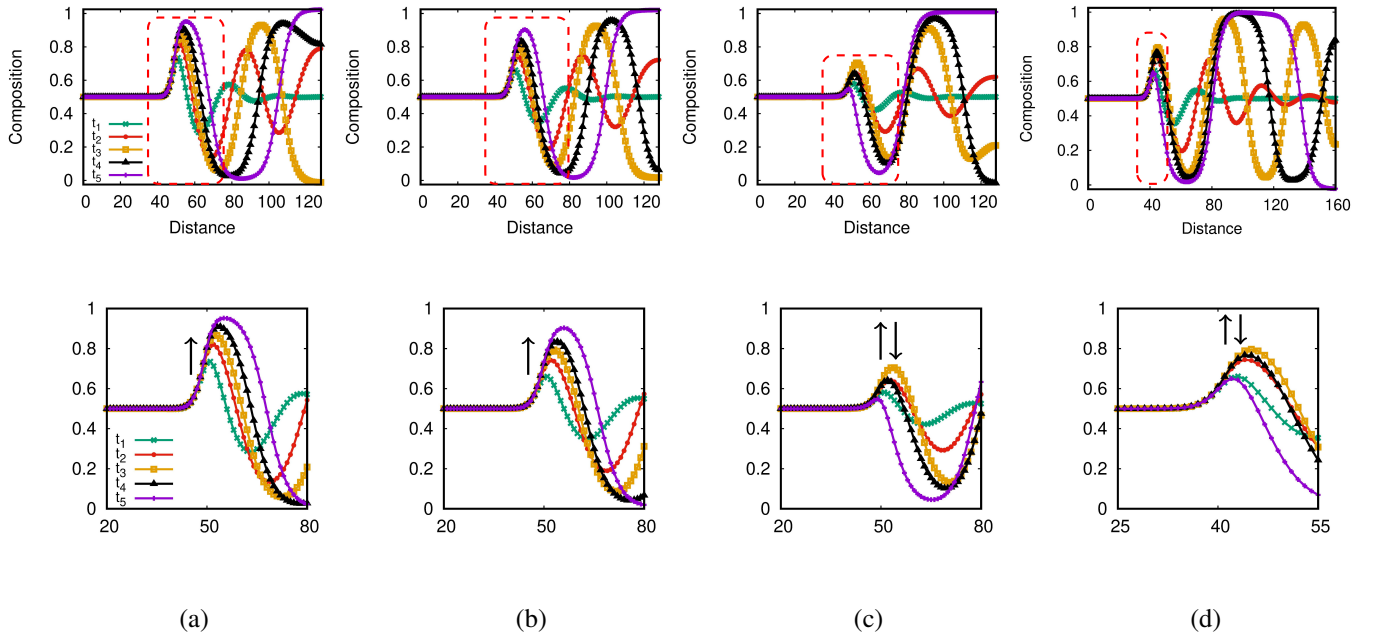


Figure 12 Top row: Evolution of radial composition line profiles drawn from matrix side into the particle. Bottom row: Magnified views of the red outlined regions in the corresponding figures above.  $t_1 < t_2 < t_3 < t_4 < t_5$ . (a)  $d = 160, \chi = 0.75$ , (b)  $d = 160, \chi = 0.5$  and (c)  $d = 160, \chi = 0.25$ , (d)  $d = 240, \chi = 0.5$ .

### Driving force for evolution of intermediate ring structures.

Ring structures develop within the circular BNPs as a result of surface-directed compositional modulation during SD. To understand the evolution and coarsening of intermediate ring structures, we need to analyze the variation of average ring size with time and correlate it with the driving force for diffusion, which in this case is the radial chemical potential gradient  $-\partial\mu/\partial r$ . For statistical quantification of phase-separated microstructures, the first zero of the pair correlation

function is often taken as a measure for the average domain size or characteristic length scale<sup>61</sup>. To determine this, we first compute the structure function  $S(\mathbf{k}, t)$  of the composition field  $c(\mathbf{r})$  by taking the Fourier transform of its spatial correlation:

$$S(\mathbf{k}, t) = \frac{1}{N} \left\langle \sum_{\mathbf{r}} \sum_{\mathbf{r}'} e^{-i\mathbf{k}\cdot\mathbf{r}} [c(\mathbf{r} + \mathbf{r}', t)c(\mathbf{r}', t) - \langle c \rangle^2] \right\rangle. \quad (9)$$

Here  $\langle \rangle$  denotes the average over the entire domain,  $N$  is the total number of grid points in the domain, and  $i = \sqrt{-1}$ . The inverse Fourier transform of  $S(\mathbf{k}, t)$  is the pair correlation function  $G(\mathbf{r}, t)$ :

$$G(\mathbf{r}, t) = \sum_{\mathbf{k}} e^{i\mathbf{k}\cdot\mathbf{r}} S(\mathbf{k}, t) \quad (10)$$

For the isotropic systems considered here, we use circular averaging of the pair correlation function and determine the location of its first zero to obtain the average ring size  $\bar{r}$  at a given time. Evolution of circularly averaged  $G(r, t)$  for  $\chi = 0.5$  is shown in Fig. 13. Except at the very early stages,  $\bar{r}$  increases continuously, indicating coarsening of rings.

Variation of  $\bar{r}$  with time, plotted in Fig. 14 in a log-log scale, reveals a step-like coarsening behavior of these rings: the plateaus correspond to a slow kinetic regime where adjacent rings have similar widths, whereas sharp changes near the end of plateaus mark an extremely fast regime in which a shrinking intermediate ring disappears due to a large gradient in concentration. The plot of  $\bar{r}$  vs.  $t$  on a logarithmic scale does not conform to the conventional power-law relation<sup>83</sup> of the type  $\bar{r}^n \propto t$ . Moreover, the plot indicates sequential, step-like coarsening of rings. We note that long range diffusion of solute is restricted here due to the formation of alternating solute-rich and solute-poor rings.

The step-like nature of coarsening dynamics within a particle is illustrated schematically in Fig. 15 where a circular particle initially contains a set of compositionally modulated rings. For this initial configuration, composition variation is shown schematically along a radial line that intersects the rings at points marked as ‘2, 3, 4, 5’; ‘1’ denotes the center of the particle. Note that the composition at these points deviate from their respective equilibrium values indicated by the blue dashed lines due to Gibbs-Thomson effect<sup>84</sup>. Since this deviation  $\Delta c \propto \sigma K$  increases with increasing interface curvature  $K$  (i.e., with decreasing radius of curvature), it gradually reduces with increasing radial distance as we move outward. Thus, it sets up a diffusion flux within each ring as shown schematically in the composition line profile (Fig. 15b). The consequent local diffusion process leads to successive coarsening and disappearance events wherein the inner rings dissolve and outer ones coarsen in a step-like fashion, depicted schematically in Figs. 15(c) and (d). When the particles are reasonably large in size,  $K$  dictates the direction of dissolution and coarsening from the center to the surface.

However, when the particle size is small, for any non-zero contact angle, the outer ring can also disappear if it has higher surface energy. For example, in a particle with size  $d = 140$  and  $\chi = 0.25$ , the outermost solute-poor  $\beta_1$  ring



dissolves while the solute-poor  $\beta_1$  core grows in size as shown in the animation in ESI. In this case, the surface energy  $\sigma$  in the Gibbs-Thomson relation dominates over interfacial curvature  $K$ , thus reversing the direction of coarsening.

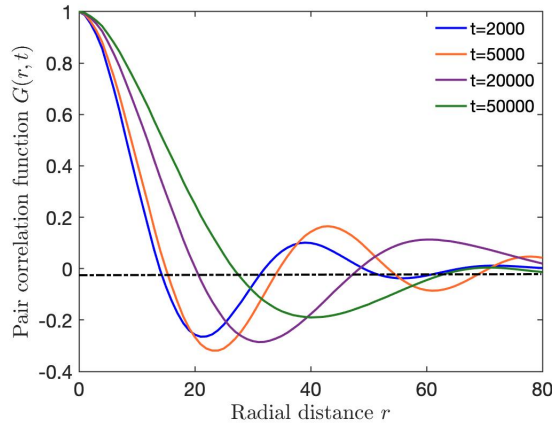


Figure 13 Evolution of circularly-averaged pair correlation function  $G(r)$  with time for  $\chi = 0.5$

Fig. 16 compares the radial variation of the driving force for solute transport  $-\partial\mu/\partial r$  within a ring for two particle sizes  $d = 140, 240$  when  $\chi = 0.5$ . It is evident from the figure that driving force for diffusion reduces considerably with increasing particle size. Hence, larger particles are more likely to exhibit metastable ‘kinetically trapped’ configurations.

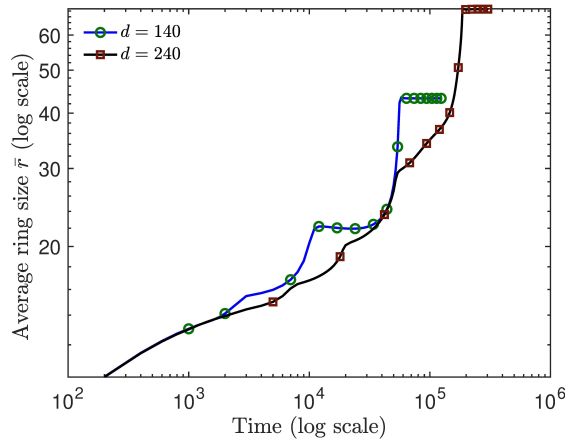


Figure 14 Evolution of average ring size with time for  $\chi = 0.5$ . To improve clarity, every third data point is marked with a circle in (a). The lines are drawn through the data points as a guide to the eye.

Note that with increasing size of the particle, bulk spinodal may also start in the interior and proceed towards the surface interfering with the radial concentration waves propagating from the surface. Here we have restricted the study to smaller sizes where bulk spinodal is negligible. This allows us to study the effect of surface-induced concentration modulations on the morphological evolution to CS/Janus structures without interference from bulk SD. When the decomposition is surface-agnostic (*i.e.*, when  $\sigma_1 = \sigma_2$ ), the equilibrium Janus does not go through an intermediate CS morphology; instead, it forms through the coarsening of domains produced by bulk SD. For all other  $\chi$  values, the time

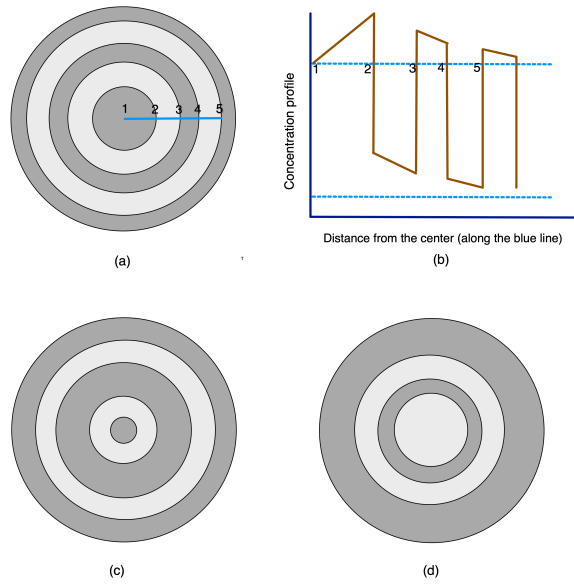


Figure 15 Schematic illustration of the step-like process of coarsening of rings. (a) Initial configuration with five compositionally modulated rings, (b) radial composition line profile, (c,d) successive disappearance and coarsening of rings.

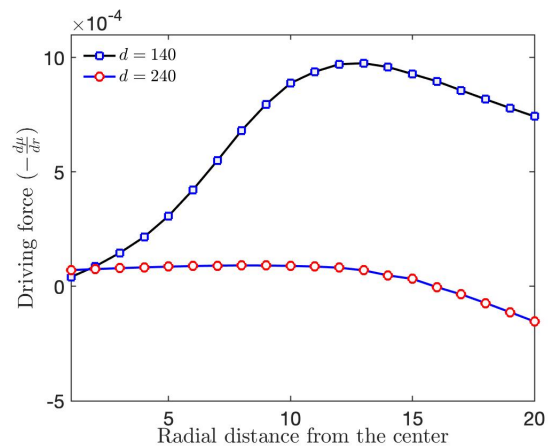


Figure 16 Variation of driving force for diffusion as function of radial distance within a single ring

taken to reach the equilibrium morphology decreases with increasing  $\chi$ .

When the contact angle is non-zero (here  $0 \leq \chi < 0.75$ ), the equilibrium configuration (based on Young's equation) is Janus. However, we observe metastable CS structures (CS-2@1 or CS-1@2) depending on the particle size and the contact angle. In all these cases, the sequence of transformation is as follows: first a solute-rich layer forms at the matrix-particle interface leading to the formation of a solute-poor layer adjacent to it. Subsequently, SDSD leads to concentric solute-rich and solute-poor rings. Later, since the innermost ring has the highest curvature, disappearance of the rings initiate from the centre of the particle. While the early-stage diffusional waves propagate from surface to centre of the particle, the late-stage dynamics propagates in the opposite direction. Evidently, the diffusional redistribution of outermost solute-lean layer during coarsening becomes more sluggish with the increase in particle size. As a result, CS morphology becomes relatively more stable with increase in particle size – CS 2@1, which requires more solute redistribution across the outermost solute-lean layer, is attained at intermediate sizes ( $d < 200$ ), whereas CS 1@2, requiring less redistribution, becomes more favourable at larger sizes.

### **Effect of particle shape on morphological evolution**

Particle shape can also modify the evolution significantly – the more the deviation from circular symmetry, the more anisotropic is the decomposition path. In Fig. 17, we demonstrate this using an elliptical particle whose area is equivalent to circular particle of  $d = 160$  with different contact angles (ESI contains the corresponding animations).

When  $\chi = 0.25$ , initial decomposition is similar to circular particle and leads to an intermediate CS-1@2 microstructure (Fig. 17d).

Since the radius of curvature of the elliptic particle is position-dependent, Gibbs-Thomson effect associated with the each layer creates an additional composition gradient along its perimeter. Simultaneously, the elongated core wants to become circular to reduce the interfacial energy. This sets up two opposing currents: (a) flux of solute towards the surface along a radial direction parallel to the major axis, and (b) flux of solute along the surface (tangential) from regions of higher curvature (poles) to those with lower curvature (equatorial points on the minor axis). This leads to a nonuniform shell thickness and an eventual pinch off of the thinnest sections at the equator (Fig. 17e). Further solute redistribution pushes the solute-poor layer towards the poles and formation of a characteristic *pole-segregated*, trimorphic structure (one of the phases at two poles separated the other phase in the equator).

When  $\chi = 0.5$ , the initial SDSD pattern remains the same. However, due to relatively larger capillarity, the solute-rich shell remains intact till later times (Fig. 17j), while a solute-lean core forms via coarsening. Eventually, the continuity of the shell disrupts, forming a pole-segregated structure. Unlike the previous  $\chi = 0.25$  case, here the poles are solute-rich and the interfaces between equatorial solute-poor phase and the polar phase is convex inwards. For complete wetting (bottom row), the initial layered structures are similar. However, coarsening produces a continuous solute-rich shell

surrounding a solute-poor core. Unlike the partial wetting case, the CS structure is retained at the later stages even though the shell thins around the equator and thickens around the poles.

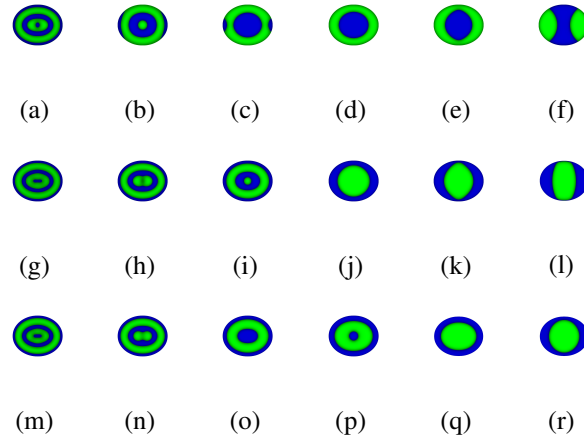


Figure 17 Time snapshots of microstructural evolution (time increasing from left to right) within an elliptic particle of aspect ratio 1.2 and area same as that of a circular particle with  $d = 160$ . Top row:  $\chi = 0.25$ , middle row:  $\chi = 0.5$ , and bottom row:  $\chi = 0.75$ . Blue and green colors represent solute-rich  $\beta_2$  and solute-poor  $\beta_1$  phases, respectively.

## 4 Conclusions

Through a systematic study, we have shown how interfacial energy and particle size interact to influence the development of CS/Janus morphology in BNPs. Fig. 18 summarizes these findings through a morphological stability map in the space of segregation parameter  $\chi$  and particle size  $d$ . Since this is not merely an equilibrium diagram but incorporates kinetic factors as well, it has a wider applicability.

The key outcomes of our study are:

1. A novel phase field method for studying morphological evolution during phase transformations in finite systems has been developed. We have applied it here to understand kinetic pathways to various configurations in BNPs.
2. The interplay of three interfacial energies, captured through the contact angle, and particle size, critically influences the development of CS, Janus and intermediate structures in BNPs. In particular, smaller size and higher contact angle tend to promote Janus, while the opposite conditions promote CS.
3. We show that discontinuous, step-like coarsening of intermediate ring structures govern the final morphology. We find that the diffusional driving force for coarsening decreases dramatically with increasing particle size, leading to kinetically trapped configurations (e.g., inverse-CS) at larger sizes.
4. For a given particle size, lower contact angle enhances the tendency to form metastable CS morphologies even when complete wetting condition given by Eq. (6) is not satisfied.

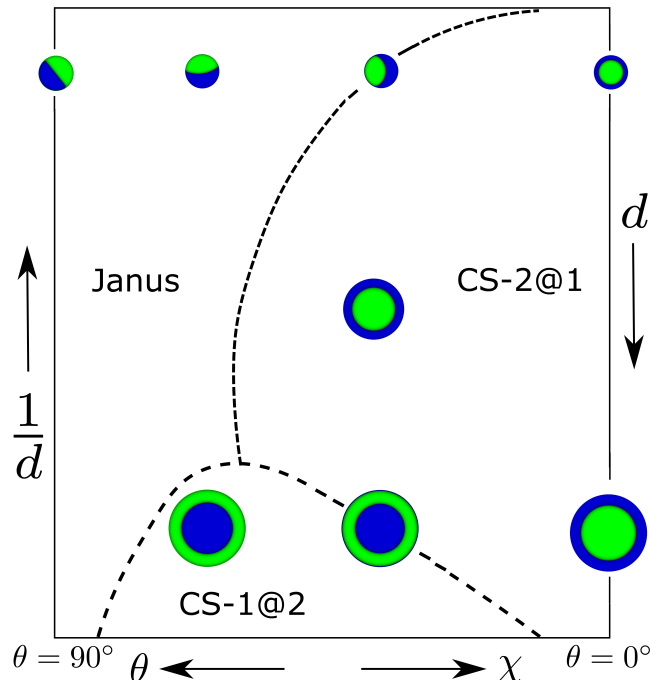


Figure 18 Morphology map in the particle size ( $d$ ) – contact angle ( $\theta$ ) space

- Our simulations with elliptical particles also highlight the possibility of attaining novel morphologies due to non-uniform particle curvature.

## 5 Acknowledgement

P.P. and S.B. gratefully acknowledge the computational support from DST Grant No. EMR/2016/006007.

## References

- [1] R. Ferrando, J. Jellinek and R. L. Johnston, *Chemical Reviews*, 2008, **108**, 845–910.
- [2] K. D. Gilroy, A. Ruditskiy, H.-C. Peng, D. Qin and Y. Xia, *Chemical Reviews*, 2016, **116**, 10414–10472.
- [3] H. Fang, J. Yang, M. Wen and Q. Wu, *Advanced Materials*, 2018, **30**, 1705698.
- [4] M. B. Cortie and A. M. McDonagh, *Chemical Reviews*, 2011, **111**, 3713–3735.
- [5] H. Zeng and S. Sun, *Advanced Functional Materials*, 2008, **18**, 391–400.
- [6] C. Langlois, Z. L. Li, J. Yuan, D. Alloyeau, J. Nelayah, D. Bochicchio, R. Ferrando and C. Ricolleau, *Nanoscale*, 2012, **4**, 3381–3388.
- [7] K. D. Malviya and K. Chattopadhyay, *The Journal of Physical Chemistry C*, 2014, **118**, 13228–13237.

- [8] C. Lee, N. R. Kim, J. Koo, Y. J. Lee and H. M. Lee, *Nanotechnology*, 2015, **26**, 455601.
- [9] J. Sopoušek, O. Zobač, J. Buršík, P. Roupčová, V. Vykoukal, P. Brož, J. Pinkas and J. Vřešťál, *Physical Chemistry Chemical Physics*, 2015, **17**, 28277–28285.
- [10] C. Srivastava, S. Chithra, K. Malviya, S. Sinha and K. Chattopadhyay, *Acta Materialia*, 2011, **59**, 6501 – 6509.
- [11] D. Wang and Y. Li, *Journal of the American Chemical Society*, 2010, **132**, 6280–6281.
- [12] A. Mayoral, D. Llamosa and Y. Huttel, *Chemical Communications*, 2015, **51**, 8442–8445.
- [13] M. Schnedlitz, M. Lasserus, R. Meyer, D. Knez, F. Hofer, W. E. Ernst and A. W. Hauser, *Chemistry of Materials*, 2018, **30**, 1113–1120.
- [14] Y. W. Lee, M. Kim, Z. H. Kim and S. W. Han, *Journal of the American Chemical Society*, 2009, **131**, 17036–17037.
- [15] J. T. McKeown, Y. Wu, J. D. Fowlkes, P. D. Rack and G. H. Campbell, *Advanced Materials*, 2015, **27**, 1060–1065.
- [16] C.-H. Jun, Y. J. Park, Y.-R. Yeon, J.-r. Choi, W.-r. Lee, S.-j. Ko and J. Cheon, *Chemical Communications*, 2006, 1619–1621.
- [17] G. Krishnan, M. A. Verheijen, G. H. Ten Brink, G. Palasantzas and B. J. Kooi, *Nanoscale*, 2013, **5**, 5375–5383.
- [18] J. Lim, H. Shin, M. Kim, H. Lee, K.-S. Lee, Y. Kwon, D. Song, S. Oh, H. Kim and E. Cho, *Nano Letters*, 2018, **18**, 2450–2458.
- [19] K. D. Malviya and K. Chattopadhyay, *Journal of Physical Chemistry C*, 2016, **120**, 27699–27706.
- [20] G. Radnóczy, E. Bokányi, Z. Erdélyi and F. Misják, *Acta Materialia*, 2017, **123**, 82–89.
- [21] C.-H. Tsai, S.-Y. Chen, J.-M. Song, I.-G. Chen and H.-Y. Lee, *Corrosion Science*, 2013, **74**, 123–129.
- [22] J. W. Cahn, *Acta Metallurgica*, 1961, **9**, 795–801.
- [23] W. T. Osowiecki, X. Ye, P. Satish, K. C. Bustillo, E. L. Clark and A. P. Alivisatos, *Journal of the American Chemical Society*, 2018, **140**, 8569–8577.
- [24] L. Tang, W. Wu, L. He, K. Yu, T. Xu, Q. Zhang, L. Zhang and L. Sun, *Journal of Physical Chemistry Letters*, 2019, **10**, 1973–1980.
- [25] N. Saunders and A. P. Miodownik, *CALPHAD (Calculation of Phase Diagrams): A Comprehensive Guide*, Pergamon, 1998.

- [26] J. Park and J. Lee, *Calphad*, 2008, **32**, 135–141.
- [27] G. Garzel, J. Janczak-Rusch and L. Zabdyr, *Calphad: Computer Coupling of Phase Diagrams and Thermochemistry*, 2012, **36**, 52–56.
- [28] M. Chu, Y. Qin, T. Xiao, W. Shen, T. Su, C. Hu and C. Tang, *Calphad*, 2021, **72**, 102233.
- [29] J. P. Hajra and S. Acharya, *Journal of Nanoscience and Nanotechnology*, 2004, **4**, 899–906.
- [30] M. A. Jabbareh and F. Monji, *Calphad*, 2018, **60**, 208–213.
- [31] L. Peng, E. Ringe, R. P. Van Duyne and L. D. Marks, *Physical Chemistry Chemical Physics*, 2015, **17**, 27940–27951.
- [32] D. Bochicchio and R. Ferrando, *Physical Review B - Condensed Matter and Materials Physics*, 2013, **87**, 165435.
- [33] M. Polak and L. Rubinovich, *Physical Chemistry Chemical Physics*, 2014, **16**, 1569–1575.
- [34] M. Chandross, *Modelling and Simulation in Materials Science and Engineering*, 2014, **22**, 075012.
- [35] H. Peng, W. Qi, S. Li and W. Ji, *Journal of Physical Chemistry C*, 2015, **119**, 2186–2195.
- [36] R. Ferrando, *Journal of Nanoparticle Research*, 2018, **20**, 1–13.
- [37] M. Fèvre, Y. Le Bouar and A. Finel, *Phys. Rev. B*, 2018, **97**, 195404.
- [38] R. Ferrando, *Structure and Properties of Nanoalloys*, Elsevier, 2016.
- [39] L. Li, X. Li, Z. Duan, R. J. Meyer, R. Carr, S. Raman, L. Koziol and G. Henkelman, *Nanoscale*, 2019, **11**, 10524–10535.
- [40] R. A. L. Jones, L. J. Norton, E. J. Kramer, F. S. Bates and P. Wiltzius, *Physical Review Letters*, 1991, **66**, 1326–1329.
- [41] S. Puri and K. Binder, *Physical Review A*, 1992, **46**, R4487–R4489.
- [42] L.-Q. Chen, *Annual Review of Materials Research*, 2002, **32**, 113–140.
- [43] W. C. Johnson and S. M. Wise, *Applied Physics Letters*, 2002, **81**, 919–921.
- [44] P. Das, P. K. Jaiswal and S. Puri, *Phys. Rev. E*, 2020, **102**, 012803.
- [45] H. Ramanarayan and T. A. Abinandanan, *Acta Materialia*, 2003, **51**, 4761–4772.
- [46] H. Ramanarayan and T. Abinandanan, *Acta Materialia*, 2004, **52**, 921–930.

- [47] S. Ghosh, A. Mukherjee, T. A. Abinandanan and S. Bose, *Phys. Chem. Chem. Phys.*, 2017, **19**, 15424–15432.
- [48] W. Johnson, *Acta Materialia*, 2001, **49**, 3463–3474.
- [49] J. W. Cahn and J. E. Hilliard, *The Journal of chemical physics*, 1958, **28**, 258–267.
- [50] S. M. Allen and J. W. Cahn, *Acta Metallurgica*, 1976, **24**, 425–437.
- [51] J. Kim and H. G. Lee, *Computers & Fluids*, 2011, **44**, 178–186.
- [52] Y. Li, J.-I. Choi and J. Kim, *Journal of Computational Physics*, 2016, **323**, 1–16.
- [53] J. W. Cahn, *The Journal of Chemical Physics*, 1977, **66**, 3667–3672.
- [54] R. Mittal and G. Iaccarino, *Annual Review of Fluid Mechanics*, 2005, **37**, 239–261.
- [55] A. Bueno-Orovio, V. M. Pérez-García and F. H. Fenton, *SIAM Journal on Scientific Computing*, 2006, **28**, 886–900.
- [56] X. Li, J. Lowengrub, A. R Ratz and A. Voigt, *Communications in Mathematical Sciences*, 2009, **7**, 81 – 107.
- [57] H. C. Yu, H. Y. Chen and K. Thornton, *Modelling and Simulation in Materials Science and Engineering*, 2012, **20**, 075008.
- [58] S. O. Poulsen and P. W. Voorhees, *International Journal of Computational Methods*, 2018, **15**, 1850014.
- [59] S.-L. Wang, R. F. Sekerka, A. A. Wheeler, B. T. Murray, S. R. Coriell, R. J. Braun and G. B. Mcfadden, *Physica D*, 1993, **69**, 189–200.
- [60] H. Strandlund, J. Odqvist and J. Ågren, *Computational Materials Science*, 2008, **44**, 265–273.
- [61] J. Zhu, L.-Q. Chen, J. Shen and V. Tikare, *Physical Review E*, 1999, **60**, 3564–3572.
- [62] D. A. Cogswell, *PhD thesis*, Massachusetts Institute of Technology, 2010.
- [63] M. Frigo and S. G. Johnson, *Proceedings of the IEEE*, 2005, **93**, 216–231.
- [64] C. Huang, M. Olvera De, L. A. Cruz and P. W. Voorhees, *Acta Materialia*, 1999, **47**, 4449–4459.
- [65] M. Hennes, J. Buchwald, U. Ross, A. Lotnyk and S. G. Mayr, *Physical Review B*, 2015, **91**, 245401.
- [66] L. Tang, W. Wu, L. He, K. Yu, T. Xu, Q. Zhang, L. Zhang and L. Sun, *Journal of Physical Chemistry Letters*, 2019, **10**, 1973–1980.
- [67] Z. Zhao, F. H. Wang, A. Fisher, Y. Shen and D. Cheng, *Journal of Alloys and Compounds*, 2017, **708**, 1150–1160.



- [68] D. Bochicchio, R. Ferrando, E. Panizon and G. Rossi, *Journal of Physics Condensed Matter*, 2016, **28**, 64005.
- [69] G. Wang, M. Van Hove, P. Ross and M. Baskes, *Progress in Surface Science*, 2005, **79**, 28 – 45.
- [70] H. G. Lee and J. Kim, *Computers and Fluids*, 2011, **44**, 178–186.
- [71] Y. H. Xu and J. P. Wang, *Advanced Materials*, 2008, **20**, 994–999.
- [72] D. Cheng, W. Wang and S. Huang, *Journal of Physical Chemistry B*, 2006, **110**, 16193–16196.
- [73] F. Baletto, C. Mottet and R. Ferrando, *Physical Review Letters*, 2003, **90**, 4.
- [74] D. Cheng and D. Cao, *Chemical Physics Letters*, 2008, **461**, 71–76.
- [75] L. O. Paz-Borbón, A. Gupta and R. L. Johnston, *Journal of Materials Chemistry*, 2008, **18**, 4154–4164.
- [76] C. W. Yuan, S. J. Shin, C. Y. Liao, J. Guzman, P. R. Stone, M. Watanabe, J. W. Ager, E. E. Haller and D. C. Chrzan, *Applied Physics Letters*, 2008, **93**, 193114.
- [77] P. Lu, M. Chandross, T. J. Boyle, B. G. Clark and P. Vianco, *APL Materials*, 2014, **2**, 0–6.
- [78] Q. Zhang, M. Xu, X. Liu, W. Zhao, C. Zong, Y. Yu, Q. Wang and H. Gai, *Chemical Communications*, 2016, **52**, 5015–5018.
- [79] J. T. McKeown, Y. Wu, J. D. Fowlkes, P. D. Rack and G. H. Campbell, *Advanced Materials*, 2015, **27**, 1060–1065.
- [80] R. Ferrando, *Journal of Physics Condensed Matter*, 2015, **27**, 13003.
- [81] L. Peng, R. P. Van Duyne and L. D. Marks, *The Journal of Physical Chemistry Letters*, 2015, **6**, 1930–1934.
- [82] B. D. Gajdics, J. J. Tomán, F. Misják, G. Radnóczy and Z. Erdélyi, *Defect and Diffusion Forum*, 2018, **383**, 89–95.
- [83] J. W. Martin, R. D. Doherty and B. Cantor, *Stability of Microstructure in Metallic Systems*, Cambridge University Press, 2nd edn, 1999.
- [84] D. A. Porter and K. E. Easterling, *Phase Transformations in Metals and Alloys*, Chapman & Hall, 2nd edn, 1992.